Anomalous ultrafast heat transfer in single palladium nanocrystals seen with an X-ray free electron laser

David Yang,[1,*] James Wrigley,[2] Jack Griffiths,[1] Longlong Wu,[1,†] Ana F. Suzana,[1,‡] Jiecheng Diao,[3,§] Angel Rodriguez-Fernandez,[2] Joerg Hallmann,[2] Alexey Zozulya,[2] Ulrike Boesenberg,[2] Roman Shayduk,[2] Jan-Etienne Pudell,[2] Anders Madsen,[2] and Ian K. Robinson[1,3,¶]

[1] *Condensed Matter Physics and Materials Science Department, Brookhaven National Laboratory, Upton, NY 11973, USA*

[2] *European X-Ray Free-Electron Laser Facility, Holzkoppel 4, 22869 Schenefeld, Germany*

[3] *London Centre for Nanotechnology, University College London, London WC1E 6BT, United Kingdom.*

(Dated: September 1, 2025)

Abstract

We report transient highly strained structural states in individual palladium (Pd) nanocrystals, electronically heated using an optical laser, which precede their uniform thermal expansion. Using an X-ray free-electron laser probe, the evolution of individual 111 Bragg peaks is measured as a function of delay time at various laser fluences. Above a laser fluence threshold at a sufficient pump-probe delay, the Bragg peak splits into multiple peaks, indicating heterogeneous strain, before returning to a single peak, corresponding to even heat distribution throughout the lattice expanded crystal. Our findings are supported by a lattice displacement and strain model of a single nanocrystal at different delay times, which agrees with the experimental data. Our observations have implications for understanding femtosecond laser interactions with metals and the potential photo-catalytic performance of Pd.

Keywords: palladium, coherent x-ray diffraction imaging, nanocrystal, heat transfer

* dyang2@bnl.gov

† Present address: Shanghai Advanced Research Institute, Chinese Academy of Sciences, Shanghai 201210, China.

‡ Present address: Chemical Sciences and Engineering Division, Argonne National Laboratory, Lemont, IL, 60439, United States

§ Present address: Center for Transformative Science, ShanghaiTech University, Shanghai 201210, China.

¶ i.robinson@ucl.ac.uk

I. INTRODUCTION

The advent of X-ray free-electron lasers (XFELs) has revolutionised the study of ultrafast structural dynamics in materials: hard X-rays are intense enough to measure diffraction from single nanocrystals in a single pulse [1]. Metallic nanocrystals are intriguing because they exhibit unique electronic, optical, and catalytic properties governed by their size, shape, surfaces, and lattice dynamics [2]. Palladium (Pd) nanocrystals, in particular, play a crucial role in catalysis, hydrogen storage, medicine, and plasmonics [3]. Yet, their non-equilibrium structural response to optical excitation remains poorly understood at ultrafast timescales and has only been addressed using molecular dynamics (MD) simulations [4]. For Pd, this non-equilibrium structural response affects energy dissipation pathways, which are crucial for optimising photo-catalytic applications [5].

Optical excitation of metals triggers rapid electron thermalisation on a femtosecond (fs) timescale, followed by electron-phonon coupling that transfers energy to the lattice over picoseconds (ps) [6]. By combining femtosecond X-ray pulses with optical laser excitation, stroboscopic "pump-probe" techniques can capture transient structural changes in metallic nanocrystals on picosecond timescales. This methodology has been critical for understanding phenomena such as coherent phonon oscillations [7], and for sufficiently high heating rates, lattice melting [8–13]. Moreover, ultrafast X-ray diffraction enables the study of thin film heterostructures, revealing heat transfer pathways between metals with different electron-phonon coupling parameters [14, 15].

Several other ultrafast time-resolved methods have been used to study heat transfer in metals. Time-resolved X-ray absorption near-edge structure (XANES) on a copper thin film has revealed the loss of crystallinity on the order of 1 ps pump-probe delay [16]. Optical reflectivity measurements on aluminium (Al) thin films demonstrate the transfer of heat from the photoexcited electrons to the lattice on the order of 2 ps delay [17]. Al thin films have also been studied using femtosecond electron diffraction, revealing a short-range order liquid structure after 3.5 ps delay under a laser fluence of 70 mJ/cm^2, providing evidence for electron-phonon coupling-mediated melting [18]. Ultrafast electron diffraction has also been applied to gold (Au) thin films to reveal heterogeneous to homogeneous melting pathways [19].

Here, we probe the transient structural states of Pd nanocrystals excited by an 800 nm

optical laser (Fig. 1). Two-dimensional (2D) 111 coherent X-ray diffraction patterns from individual nanoparticles were measured at various delay times and laser fluences ranging from $57 - 230$ mJ/cm^2. By monitoring the Bragg peak positions, we can infer that a macroscopic, out-of-plane rotation of the crystal takes place after pumping. Using coherent imaging results, we generate a distinct model of the heterogeneous lattice strain distribution within one of the crystals, which we attribute to the inhomogeneous distribution of electrons generated by the laser. This model illustrates the build-up of a strain distribution with simultaneously compressed and expanded regions within a single nanocrystal, lasting approximately 20 ps.

The two-temperature model (TTM) has been frequently used to describe the response of a material to a femtosecond laser pulse [20]. The laser heats electrons on the surface of a metal crystal to a very high temperature. This heat is then transferred to the crystal lattice first by electron diffusion, and then by electron-phonon coupling to the lattice over a few picoseconds. The spatial distribution of the heat transfer throughout the crystal depends on the mean free path of electrons, which is both temperature and material-dependent [21]. The leading model for the melting of bulk polycrystalline materials is a heterogeneous to homogeneous pathway [9, 19, 22], involving atoms at defects, surfaces, and grain boundaries becoming disordered first, followed by the rest of the crystal volume at the timescale dictated by thermal diffusion. On which timescales these events take place in a single nanocrystal is addressed by the results of the experiments described here: the electrons get optically heated and travel only partway through the crystal, upon which they then transfer heat to the lattice and cause heterogeneous strain.

Previous studies have demonstrated that intense optical excitation induces non-thermal melting, especially in semiconductors [23]. In thin polycrystalline Pd films, the transition from crystalline to liquid states proceeds heterogeneously via grain boundaries before evolving into homogeneous melting at higher fluences [9, 10, 19, 22, 24]. Lattice compression lasting tens of picoseconds, found in Pd [10] and Pt [25] films, is an important signature of inhomogeneity of the thermal distribution [26]. A similar study performed on Au thin films [8] did not reveal any compressive response, while this was seen in Cu [27] at high laser fluences of a long-pulse drive laser. Unlike the previous ensemble-averaged measurements, individual Au nanocrystals have been studied using similar optical laser pump-XFEL probe experiments, and did not show any signs of compression [7, 11]. By analogy with the thin film results, the melting pathway of isolated Pd nanocrystals reported in this work is ex-

pected to differ from Au nanocrystals since the electron-phonon coupling rate is greater for Pd [28].

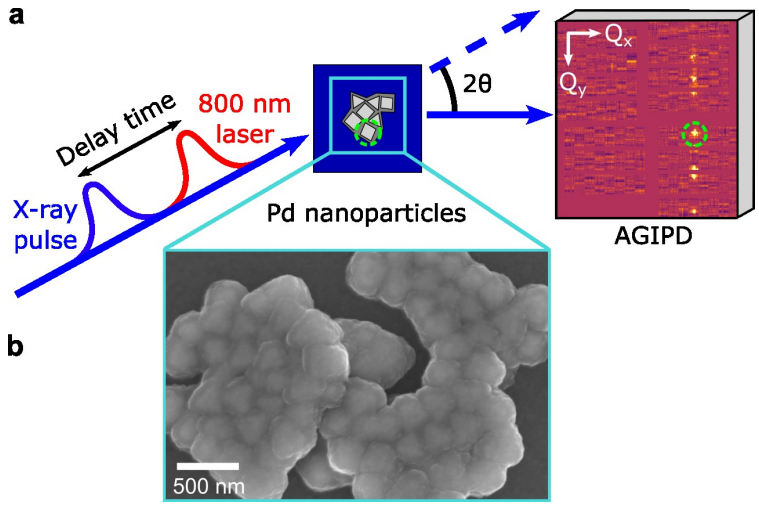

FIG. 1. Experimental ultrafast pump-probe X-ray diffraction setup in horizontal scattering geometry. **a** The samples are pumped using an 800 nm optical laser, followed by an X-ray probe with a variable delay. An isolated 111 Bragg peak, corresponding to a single Pd nanoparticle (green dashed circle), was measured using the adaptive gain integrating pixel detector (AGIPD) positioned 4 m from the sample at 2θ. White arrows indicate the Q_x and Q_y directions in reciprocal space. **b** SEM image of octahedral-shaped Pd nanocrystals coated with $\sim$ 10 nm of TiO_2 for stability and fixed on a Si substrate using tetraethyl orthosilicate (TEOS). The lighter, triangle-shaped profiles show the Pd particle facets, surrounded by the darker TiO_2 coating.

II. RESULTS

We first report the pump-probe X-ray diffraction patterns for three Pd nanoparticles, labelled as crystals A-C, at different optical laser fluences and delay times. Different crystals were selected from the composite shown in Fig.1b. The evolution of the 111 2D Bragg peak for crystal A at select delay times is shown in Fig. 2. The optical laser pump was timed to coincide with alternating collinear X-ray probe pulses of the XFEL. Analogous data for crystals B and C are in Figs. S2 - S4. Before the measurement, the diffraction was aligned to the maximum of its rocking curve without laser pumping. For crystal A, the measurements were performed sequentially, from low to high laser fluence, alternating

between laser-pumped and unpumped XFEL pulses (Methods). Unpumped pulses for crystal A, shown in Fig. S1, proved that the crystal returns to its original state after each laser pulse at all fluences.

At the lowest measured laser fluence, 57 mJ/cm^2, there were slight horizontal translations of the Bragg peak position on the detector, denoting changes in the Bragg angle (θ) but the peak shape was relatively unchanged. At a laser fluence of 110 mJ/cm^2, we observed a slight splitting of the Bragg peak at 30 ps delay, which then resumes as a single peak after 50 ps, though shifted in peak position ($Q_{x,y}$). This was followed by relative peak translations and some Bragg peak disorder, relative to the lowest laser fluence. For the next laser fluence, 170 mJ/cm^2, there was a more pronounced peak splitting and disorder, following the same timeline as observed for 110 mJ/cm^2. This clear splitting is not apparent at later delay times, which we attribute to damping. However, we note a strong decrease in Bragg peak intensity, particularly at 90 ps and 210 ps. A drop in Bragg peak intensity at positive delay times is most evident at 230 mJ/cm^2.

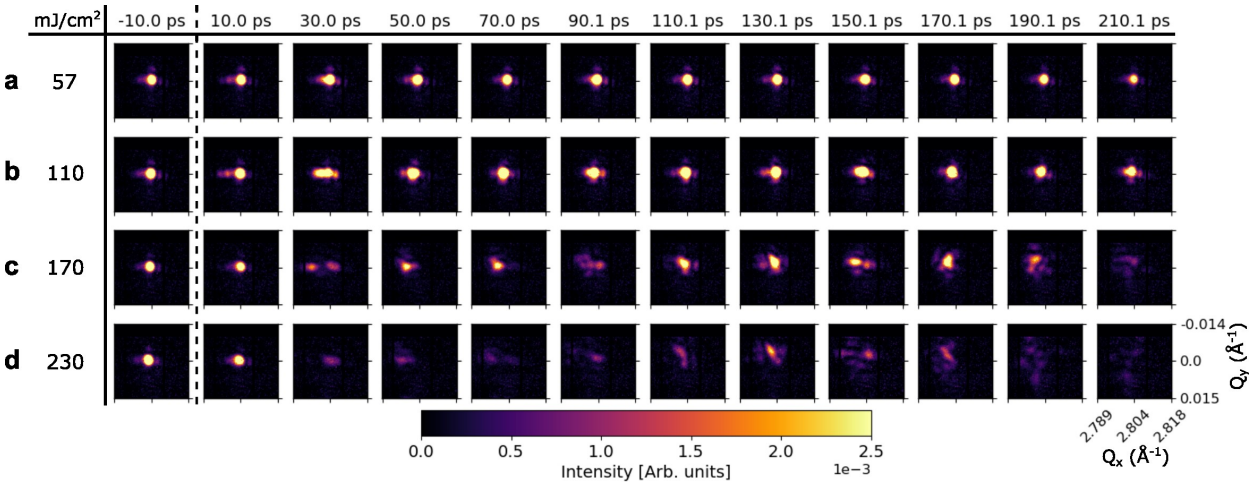

FIG. 2. Evolution of the 111 Bragg peak intensity on a linear scale for crystal A at various delay times and laser fluences. Rows **a** - **d** correspond to sequential delay measurements using different fluences. The evolution of crystals B and C is shown in Figs. S2 - S4.

Small vertical peak shifts can be interpreted as the rotation of the crystals, while small peak shifts along the horizontal direction (2θ) are due to changes in the average lattice parameter. The change in average lattice relative to its unperturbed state at negative delay times represents a homogeneous strain. Heterogeneous strain, relative to the average lattice,

can be inferred from the changes in the full width at half maximum (FWHM) of the Bragg peak line profile. The FWHM provides information about the local distortion of the crystal lattice.

A. Incoherent imaging

To quantify the evolution of the Bragg peaks, they were approximated as 2D Gaussian functions (Methods). The χ^2 error of the Gaussian fitting for crystal A is shown in Fig. S5–only fits with a $\chi^2 < 0.3$ were considered for analysis. The fitted peak positions and FWHM along the horizontal detector direction, Q_x, are plotted as a function of delay time in Fig. 3(i).

We observe an initial homogeneous compression of the crystal between 0 to 20 ps above 57 mJ/cm^2 in Fig. 3a(i) and c(i). Then, the crystal expands in an oscillatory pattern for the remainder of the delay scan. We see a prominent oscillation along the horizontal direction, fitted using Eq. S1, showing a period of $\sim$ 120 ps (Fig. 3a(i)). This corresponds to crystal A's lowest-frequency vibrational mode, the "breathing mode". As the laser fluence increases, we observe an increase in the oscillation amplitude of the Bragg peak position. The increased laser fluence also causes greater homogeneous lattice expansion, as seen in the greater displacement in the horizontal direction.

In Fig. 3a-c(ii), we observe oscillations in the horizontal FWHM, ΔQ_x, of the Gaussian-fitted crystals. Using the fitting function shown in Eq. S2, we observe an oscillation with a period of 60 ps, most apparent for a laser fluence of 110 mJ/cm^2. Interestingly, this is half the period of the 120 ps breathing mode, corresponding to the acoustic wave propagating forwards and backwards through the crystal [29]. The horizontal FWHM is a measure of the presence of heterogeneous strain, which would be greatest when the acoustic wave lies halfway through the crystal, occurring twice per acoustic wave period.

To test the reproducibility of our observations, we measured two other crystals, A and C, at laser fluences of 57 mJ/cm^2 and 110 mJ/cm^2. The Bragg peaks again were fitted as 2D Gaussian functions, and the resulting centre of masses and FWHMs are plotted as a function of delay time, shown in Fig. 3b and c. The period of the oscillations in the horizontal direction is consistent for both laser fluences and all crystals, and the oscillation amplitudes increase for all crystals as the laser fluence increases.

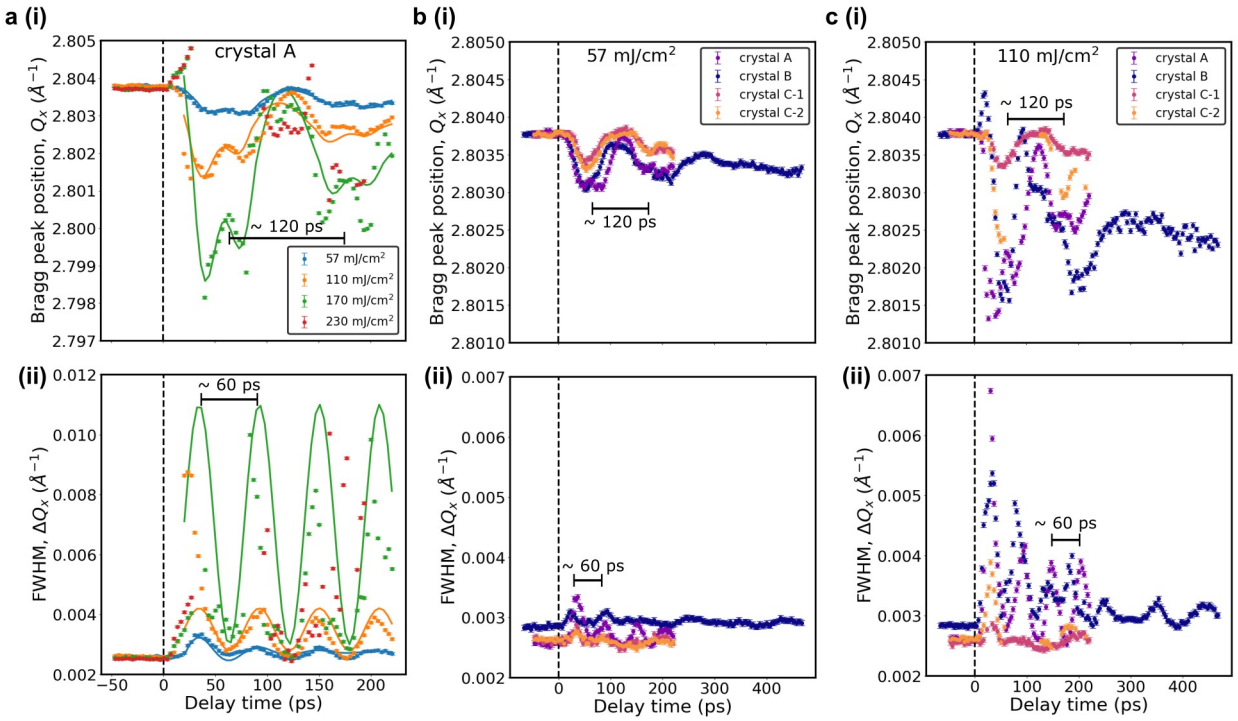

FIG. 3. Summary of the changes to the Gaussian-fitted Bragg peaks along the horizontal 2θ direction, Q_x, as a function of laser fluence and delay time. **a** Fitted parameters for various laser fluences for Crystal A. (i) Fitted position of the Bragg peak along Q_x. The oscillations were fitted with Eq. S1 for all fluences except for 230 mJ/cm^2 due to a lack of signal. (ii) Fitted FWHM of the Bragg peak along the horizontal direction. The oscillations were fitted with Eq. S2. The error of the Gaussian fits is shown in Fig. S5. **b** Fitted parameters for a laser fluence of 57 mJ/cm^2 on all measured crystals. **c** Fitted parameters for a laser fluence of 110 mJ/cm^2 on all measured crystals. Crystal C-1 and C-2 are two successive measurements on the same crystal. The error bars reflect two standard deviations of repeated measurements at negative delay times. Oscillation periods are shown by the horizontal bars in each panel. The error of the Gaussian fits is shown in Fig. S9 for **b** and **c**. The equivalent of this figure in the Q_y direction is Fig. S6.

The FWHM of the fitted Gaussians show similar oscillation periods along the horizontal direction, with an oscillation amplitude increasing with laser fluence. The fitted FWHM is different for each crystal, owing to slight differences in crystal morphology and initial residual strain state, but they all show similar oscillations along the horizontal direction.

The peak movements in the vertical detector direction, Q_y, are presented in Fig. S6 for all measured crystals. While no oscillations were observed, peak translations, interpreted as

rotations, were found to increase with laser fluence. The degree of rotation increases with laser fluence, up to -0.003 Å^{-1} or -0.5 mrad (~ 0.03 °) for 230 mJ/cm^2. We attribute the notable decrease in Bragg peak intensity in Fig. 2d to the selected Pd crystal being stroboscopically rotated out of Bragg condition. The crystal rotation along the rocking axis as a function of delay time was estimated from the drop in intensity by calibrating against a rocking curve, shown in Fig. S7, indicating there is a maximum rotation of ~ 0.06 °. This rotation is largely due to the lattice parameter expanding and contracting (see supplementary information).

B. Coherent imaging

We now turn to the question of the details of the strain detected in the FWHM of the diffraction patterns discussed above, paying attention to the first 50 ps. The XFEL beam used for the measurements was fully coherent, thus the diffraction can be interpreted in the language of Bragg Coherent Diffraction Imaging (BCDI) [30]. The measured BCDI patterns were sufficiently oversampled by at least twice the Nyquist frequency [31], at least 2 pixels per fringe along each dimension, so iterative phase retrieval algorithms could be used to recover the phase of the Bragg peak [32], enabling us to obtain real-space images of the sample through the Fourier transform. The corresponding phase of the real-space image represents the projection of the displacement field onto the scattering vector, $\mathbf{u_{111}}$, from which we can also determine the corresponding strain field along the same direction, ε_{111} [30].

For our measurements, which were 2D sections of the coherent diffraction patterns, the low signal-to-noise levels rendered the attempted reconstructions non-reproducible. So, as a simpler approach, a 1D forward model of the complex phase function describing crystal A was created and used to fit the measured Bragg peaks at various delay times instead (Methods). In order to explain peak splitting in the horizontal (2θ or Q_x) and little change in the vertical (Q_y) directions, we assumed a rectangular-shaped crystal (a projection of an octahedral Pd crystal in 2D) of uniform amplitude with a boundary located at $x = x_0$ inside it. Within the region $x \leq x_0$, the image phase ramps up with a positive slope, s_1, while in the region $x > x_0$, it ramps down with a negative slope, s_2 (Eq. 7). These three fit parameters were sufficient to explain the transient splitting of the peak at higher fluences

in the early delay time range (< 60 ps) and also to explain the enlarged FWHM at higher fluences. The slopes correspond to the peak shifts, while x_0 couples to the relative peak intensity of the split peak and its asymmetry at lower fluences. Following the usual BCDI convention [30], the image phase is proportional to the local lattice displacement along Q and its derivative is the local strain in the crystal. For each fluence and delay in Fig 4, we show images of the displacement in row (iii) and the strain in row (iv), as fitted to the BCDI data with this model.

In Fig. 4a, we observe that the crystal has a homogeneous displacement and relatively low strain at a laser fluence of 57 mJ/cm^2. There is no noticeable splitting in the Bragg peak, which is reflected by the homogeneous displacement in the model. At a laser fluence of 110 mJ/cm^2, shown in Fig. 4b, we observe an inhomogeneous phase starting at 6.7 ps, with side-by-side compressed and expanded regions of the crystal. The boundary between the two migrates at the speed of sound (Fig. 5c), as the delay time increases so that the compressed region gradually diminishes, leaving an expanded crystal. Interestingly, the strain is mostly negative after 16.7 ps, which could be due to thermal expansion from the region that the heat pulse has already passed through. As the laser fluence is increased to 170 mJ/cm^2, shown in Fig. 4c, we also observe the boundary propagating through the crystal at the speed of sound, responsible for the Bragg peak split around 30 ps. This time, neither of the two distinct regions of the crystal with different average lattice parameters is compressed. It may be that the higher heating rate negates the compression, or it is possibly due to the limited spatial resolution [33]. The sharper compression wave with a higher compressive strain suggests a more compressed wavefront coinciding with a higher laser fluence, leaving a slightly tensile region after the wave passes through.

Displacement and strain trends can be extracted from the model, shown in Fig. 5. The range of $\mathbf{u_{111}}$ is demonstrated in Fig. 5a. For all laser fluences, the values increase in magnitude at positive delay times. At 110 mJ/cm^2 and 170 mJ/cm^2 we observe small oscillations in the maximum and minimum $\mathbf{u_{111}}$ with a period of 20 ps. At positive delay times, the average $\mathbf{u_{111}}$ increases with increasing laser fluence (Fig. S8a). The standard deviation of $\mathbf{u_{111}}$ also increases at positive delay times (Fig. S8b), demonstrating the increased levels of lattice displacement heterogeneity.

The range of ε_{111} is demonstrated in Fig. 5b. For 57 mJ/cm^2, we only observe tensile strain, associated with lattice expansion. At 110 mJ/cm^2 and 170 mJ/cm^2, we observe both

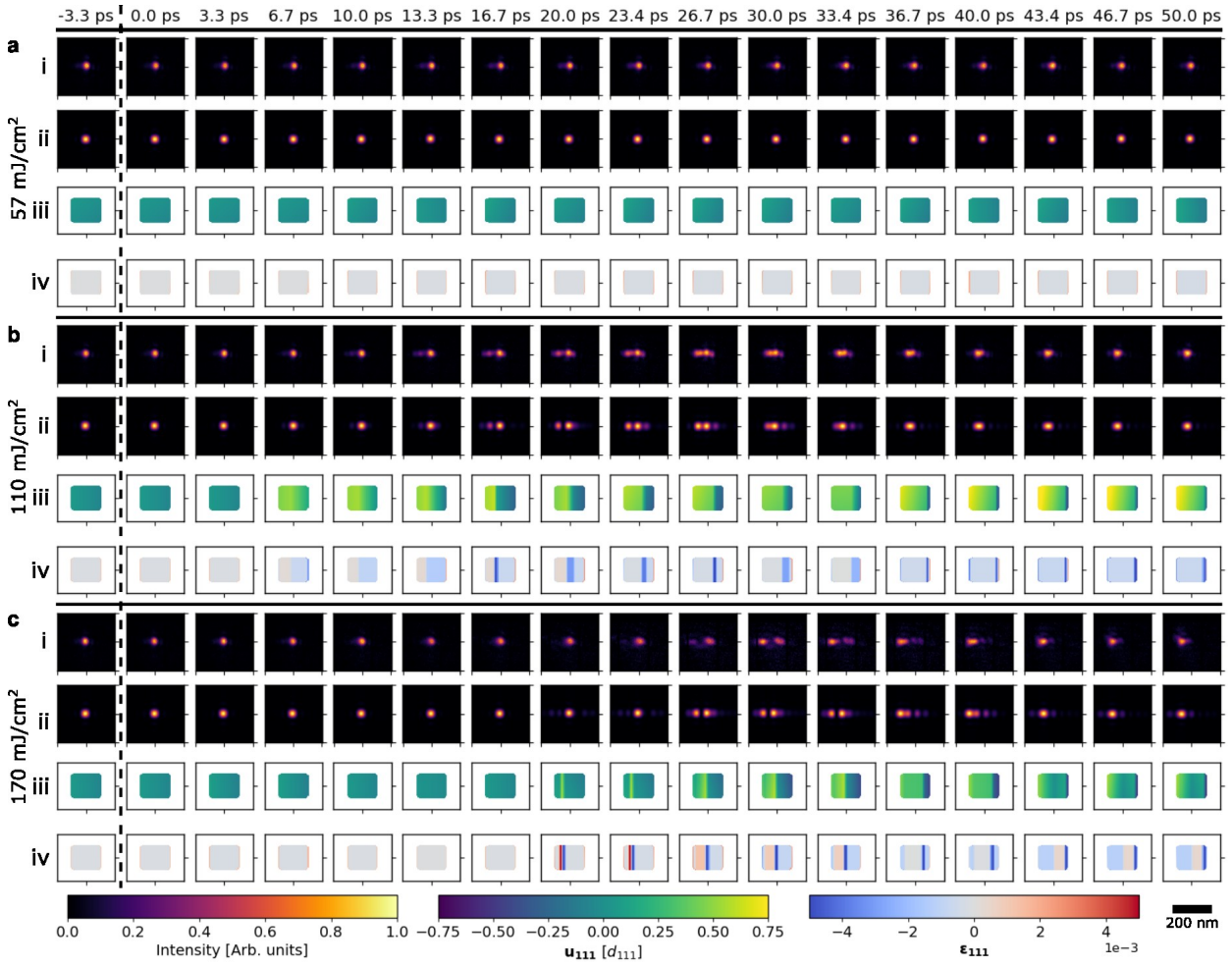

FIG. 4. Real-space 2D model of crystal A in the laboratory frame up to 50 ps delay time at **a** 57 mJ/cm^2, **b** 110 mJ/cm^2 and **c** 170 mJ/cm^2. For each subfigure, (i) the experimental Bragg peak, (ii) the model Bragg peak, (iii) the real space model displacement and (iv) the real space model strain are presented as rows. (i) and (ii) refer to the bottom left colour bar, (iii) refers to the bottom middle colour bar and (iv) refers to the bottom right bar. The experimental and model Bragg peaks are both normalised for ease of comparison. The error associated with the model is shown in Fig. S10 and the parameters are shown in Fig. 5 and Fig. S11.

tensile and compressive strains that persist at positive delay times. At positive delay times, the average ε_{111} shows an increasing compression, and the standard deviation of ε_{111} also increases (Fig. S8c and d, respectively). The latter demonstrates increased levels of strain heterogeneity.

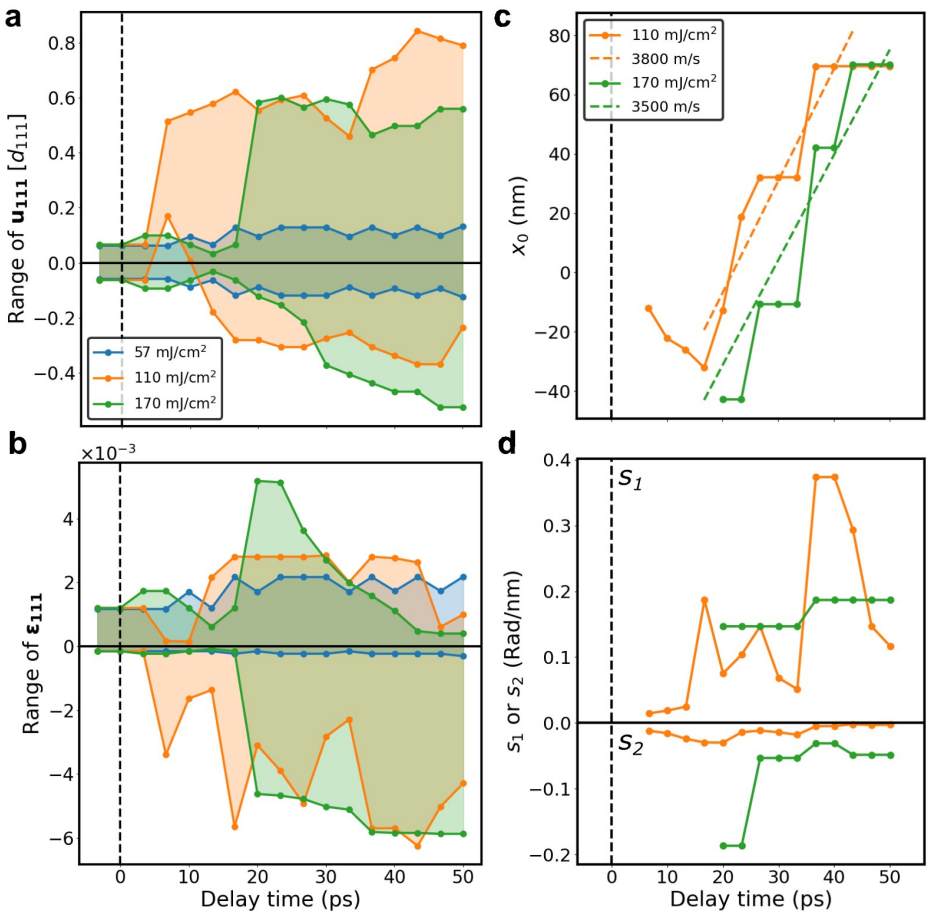

FIG. 5. The displacement, $\mathbf{u_{111}}$ and strain, ε_{111} values at different laser fluences extracted from the 2D model in Fig. 4. The maximum and minimum $\mathbf{u_{111}}$ and ε_{111} are displayed in **a** and **b**, respectively. The average and standard deviations of $\mathbf{u_{111}}$ and ε_{111} are shown in Fig. S8. The main model variables in Eq. 7: (c) wave peak position, x_0; (d) positive slope, s_1, leading to x_0, and negative slope, s_2, descending from x_0. The dashed lines in **c** show the speed of the boundary propagation.

III. DISCUSSION

A. Electron Dynamics and Heating

The results can be rationalised with the help of the TTM [20]. The 15 fs laser pulse interacts with the electrons in the Pd nanocrystal, raising them to a high temperature. The electromagnetic skin depth predicts the laser penetration into the metal, determined using Eq. 1,

$$\delta = \frac{\lambda_{\text{laser}}}{4\pi k}, \tag{1}$$

where $k = 5.09$ is the extinction coefficient for Pd [34], giving $\delta_{\text{Pd}} = 12.5$ nm. Since this is a small fraction of the 180 nm crystal size, the material within this small depth does not contribute very much to the diffracted signal. The electrons within this skin depth will be multi-photon excited to high energy states during the femtosecond pulse, creating a non-equilibrium hot electron distribution. Hot electrons can travel rapidly through the crystal before electron-phonon coupling takes place, creating phonons that heat the lattice on a picosecond timescale. The 120 ps period "breathing" mode oscillations in Fig. 3a(i) are caused by these phonons travelling back and forth across crystal A. The size of crystal A is around 180 nm, shown in the 2D model (Fig. 4). The speed of sound is therefore 180×10^{-9} m/$(120 \times 10^{-12}$ s/2) = 3000 m s^{-1}, in agreement with the reported value of 3070 m s^{-1} [35].

At higher laser fluences, most notably at 110 mJ/cm^2 and 170 mJ/cm^2, we observe Bragg peak splitting most prominently around 30 ps delay. Bragg peak splitting has been reported on $SrRuO_3$ thin films, which is caused by strain variations in different regions following laser excitation [36]. Similarly, the pronounced splitting we observe corresponds to inhomogeneous strain due to non-uniform heating of the crystal. This informs us that the hot electrons do not fully redistribute within the Pd crystal before they transfer their heat to the lattice. This leads to lattice strain at the boundary between the heated and unheated regions of the crystal (Fig. 4) as well as diffraction pattern broadening (Fig. 3a(ii)-c(ii)) and splitting (Fig. 2).

At the lowest laser fluence used in this study, 57 mJ/cm^2, we did not see signs of splitting in any of the measured Pd crystals, but a clear increase in the FWHM around 30 ps instead. These results generally agree with a previous Au nanocrystal melting study [11] that used laser fluences up to ~ 56 mJ/cm^2. For Au, the laser penetration depth is $\delta_{\text{Au}} = 13.0$ nm, assuming $k = 4.91$ [34], similar to the value for Pd. However, there is a large difference in the electron-phonon coupling parameter, with Pd about five times greater than Au [28], resulting in the electron mean free path of hot electrons being larger in Au than Pd. Therefore, the laser-heated electrons distribute throughout a larger volume of an Au nanocrystal before interacting with the lattice, heating the crystal relatively uniformly and reducing the likelihood of peak broadening or splitting. Additionally, the electronic specific heat capacity,

TABLE I. Expected homogeneous strain and temperature rise for different laser fluences.

mJ/cm^2	Homogeneous strain (%)	Temperature rise (K)
57	0.026	22
110	0.088	75
170	0.19	160
230	0.24	210

proportional to the electronic density of states at the Fermi level, is about 16 times larger for Pd [37] than for Au [38]. For a given energy, the electrons in Au will reach higher temperatures than those in Pd, creating a larger temperature gradient and thus faster thermal transport from the hot electrons to the lattice.

The expected average temperature rise in the crystal, ΔT, due to one laser pulse can be estimated by $\Delta T = e_{111}/\alpha_{\mathrm{Pd}}$, where e_{111} is the homogeneous strain and $\alpha_{\mathrm{Pd}} = 11.8 \times 10^{-6}$ K^{-1} is the coefficient of linear thermal expansion. The homogeneous strain is defined in Eq. 2,

$$e_{111} = \frac{Q_0 - Q}{Q_0}, \tag{2}$$

where $Q_0 = 2.8038$ Å^{-1} is the value at negative delay times, shown in Fig. 3a(i). The tensile strain and corresponding maximum rise in temperature are shown in Table I. These average temperatures are well below the melting temperature of Pd.

B. Compressive effects

This compression due to pressure build-up from pulsed laser heating has been previously reported in Pd thin films [10]. For crystal A, in Fig. 3, we observe a compression of the average lattice constant between 0 to 20 ps at 170 mJ/cm^2 and 230 mJ/cm^2. Using Eq. 2, this corresponds to a compressive strain of -0.025 % and -0.032 %, respectively. This is consistent with a previous study on Pd thin films with a laser fluence of 800 mJ/cm^2, which revealed a maximum compression of -0.032 % at 20 ps [10].

The coherent diffraction results allow the compression to be visualised directly in the

model images of Fig. 4. The effect is clearest at 110 mJ/cm^2 in Fig. 4b and appears to be overwhelmed by larger expansions at higher fluences. It appears that because of the inhomegeneous electron heating, only the front part of the crystal facing the laser expands to create a pressure wave that compresses the back of the crystal. As thermal diffusion causes the temperature to equilibrate, the boundary between the expanded and compressed regions is seen to have migrated through the crystal after 50 ps.

According to Fick's law of diffusion, the heat flow is proportional to the temperature gradient. The solution to the one-dimensional heat equation predicts a Gaussian distribution from an impulse of heat at time $t = 0$, with a thermal diffusion width, w,

$$w = \sqrt{\frac{2k_T t}{C_p \rho}}, \tag{3}$$

where k_T is the thermal conductivity (72 W m^{-1} K^{-1}), C_p is the specific heat capacity (240 J kg^{-1} K^{-1}) and ρ is the density (12 g cm^{-3}) [35]. The thermal equilibration time of a 180 nm Pd crystal is therefore expected to be 650 ps, which is longer than the observed elastic wave takes to propagate through the crystal (at the speed of sound), taking 60 ps to travel 180 nm. We conclude that in the ultrafast nanoscale regime, after optical excitation, we have no local thermal equilibrium between electrons and phonons. Hot electron transport alters the energy distribution within the sample, thereby determining the observed strain dynamics. Within the first $\sim$ 60 ps, classical thermal diffusion would predict that only 55 nm of the crystal would be heated, which is not what we observe. Thus, the TTM provides a more accurate representation of the time and length scales governing our observations of heat transfer.

IV. CONCLUSION

We have presented the results of an optical laser pump and coherent X-ray diffraction probe experiment to reveal nonequilibrium lattice dynamics in isolated Pd nanocrystals. These results show laser fluence-dependent changes in the heating of Pd nanocrystals at different delay times. We documented a diffraction peak splitting that occurs around 30 ps delay, which reveals uneven heating of the nanocrystal. This was not seen in previous studies on isolated Au nanocrystals of similar size [7, 11]. We attribute the observed inhomogeneity due to hot electrons in Pd having a shorter mean free path and Pd possessing a higher

electronic specific heat capacity compared to Au. The uneven heating induces a lattice strain distribution, visualised by fitting a coherent diffraction model to the data. Our ability to image the mechanisms involved in heat transfer through lattice strain allows us to gain a better understanding of fundamental heat transport in single nanocrystals. This has applications in predicting reaction rates and preventing thermal degradation in photocatalysis [5].

V. METHODS

A. Sample synthesis

Octahedral-shaped palladium nanocrystals (Fig. 1) were synthesised using a seed-mediated approach. The procedure is described here, reproduced from our previous study [39]. Nanocrystals were first prepared by combining 0.500 g of CTAB, 0.5 mL of 0.01 M tetrachloropalladate(II) acid (H_2PdCl_4), 0.3 mL of 0.01 M sodium iodide (NaI), and 10 mL of nanopure water. This mixture was heated in an oil bath at 95 °C for 5 minutes. Subsequently, 200 μL of 0.04 M ascorbic acid solution was added, and the temperature was maintained at 95 °C for 1 hour. For the growth step, 0.360 g of CTAB, 0.250 mL of 0.01 M H_2PdCl_4, 0.050 mL of 0.001 M NaI, and 9.375 mL of nanopure water were combined and kept at 30 °C. After 5 minutes, 80 μL of the previously prepared Pd seed solution and 250 μL of 0.04 M ascorbic acid solution were introduced. The reaction was then allowed to proceed at 30 °C for 40 hours. Crystalline TiO_2 coatings were deposited using a Cambridge Nanotech Savannah 100 system. The deposition was carried out at 500 °C under a continuous Ar flow of 20 sccm (base pressure approximately 100 mTorr). Titanium isopropoxide ($Ti(iPrO)_4$), heated to 75 °C, served as the titanium precursor, while nanopure water at room temperature acted as the oxygen source. The pulse and purge times were 0.1 s and 5 s for $Ti(iPrO)_4$, and 0.01 s and 10 s for H_2O, respectively. The nanocrystals were drop-cast onto a single-crystal Si wafer and then fixed with tetraethyl orthosilicate (TEOS) [40].

B. X-ray free-electron laser experiments

Coherent X-ray diffraction experiments were performed at the Materials Imaging and Dynamics (MID) instrument at the European XFEL [41]. All measurements were performed

using horizontal scattering geometry. We used a self-seeded X-ray with a bandwidth of ~ 1 eV centred at 9 keV with 0.67% transmission. The X-ray was focused to a 4 μm spot size using compound refractive lenses (CRLs). The repetition rate of the X-ray pulses in a train was 2.25 MHz, and the trains were delivered at 10 Hz with 60 pulses per train. At each delay motor position data for 6 seconds (60 trains) were taken. The exposure time was 20 nanoseconds. Only the first pulse per train was used for the data analysis. The 111 Bragg peaks of single Pd nanocrystals were measured on an adaptive gain integrating pixel detector (AGIPD) [42], with a detector pixel size of 200 μm, positioned 4 m from the sample at $2\theta = 35.8°$. The optical laser delivered 15 fs pulses with a central wavelength of 800 nm matching the X-ray pulse pattern. It was focused to a 20 μm spot size at the sample position. All delay measurements, except for those performed on crystal B, were performed stroboscopically, alternating between pumped and unpumped X-ray pulses.

C. Data processing

Calibrated raw data were processed using DAMNIT [43]. The intensity was normalised using the X-ray gas monitor (XGM) [44] intensity at each frame before taking the mean of the first pulses of each pumped pulse train at each delay motor position. For each crystal, the detector image was cropped to an array of 128×128 such that the Bragg peak was in the centre of the array at negative delay times. The cropping region was fixed for each crystal at positive delay times. The mean of a 20×20 pixel area in the corner of each cropped image was determined as the background level, which was then subtracted from each cropped image.

D. Gaussian fitting

The `curve_fit` function from the Python `scipy.optimize` library [45] was used to fit the measured Bragg peaks to a 2D Gaussian function. The 2D Gaussian function, which represents the Bragg peak intensity, I_{fit}, is shown in Eq. 4,

$$I_{\text{fit}}(x, y) = A_0 \exp\left(-\frac{1}{2}\left[\frac{(x-\mu_x)^2}{\sigma_x^2} + \frac{(y-\mu_y)^2}{\sigma_y^2}\right]\right) + O, \tag{4}$$

where A_0 is the amplitude, $\mu_{x,y}$ are the pixel coordinates of the Bragg peak centre, $\sigma_{x,y}$ are

the widths in pixels of size $p = 200$ μm, and O is the background offset. The Bragg peak position is determined as $Q_{x,y} = \frac{2\pi p}{\lambda d}\mu_{x,y} + \frac{4\pi}{\lambda}\sin(\theta)$, where $\lambda = 1.378$ Å at 9 keV, $d = 4$ m, $\theta = 17.9$ °. The FWHM in reciprocal space units is computed as $\Delta Q_{x,y} = \frac{4\pi p}{\lambda d}\sigma_{x,y}\sqrt{2\ln 2}$.

The χ^2 error was computed on a 64×64 array at the centre of the 128×128 array using Eq. 5,

$$\chi^2 = \sum^{n} \frac{(\sqrt{I_{\text{fit}}} - \sqrt{I_{\text{measured}}})^2}{I_{\text{measured}}}, \tag{5}$$

where n corresponds to each pixel in the 64×64 array and I_{measured} is the measured Bragg peak intensity.

E. Modelling of the internal structure of a Pd nanoparticle

We assume an initial shape of a rounded rectangle to give a Bragg peak similar to the shape shown at negative delay times. This assumption is not unreasonable, as the Pd nanoparticles resemble octahedral shapes, as shown in a previous study [39], thus a rectangle could be representative of its projection in 2D. The shape parameters were optimised with boundary conditions using the `minimize` function from the Python `scipy.optimize` library [45]. The correlation between the normalised intensity of the model, $|\mathcal{F}(S(r))|^2$, and the measured normalised intensity was maximised. This was achieved by minimising $1 - r$, where r is the Pearson correlation coefficient computed using the `pearsonr` function from `scipy.stats` [45]. This metric was used to account for any Bragg peak intensity normalisation uncertainties. r is also shown in Eq. 6,

$$r(x,y) = \frac{\sum\limits_{n}(x_n - \bar{x})(y_n - \bar{y})}{\sqrt{\sum\limits_{n}(x_n - \bar{x})^2}\sqrt{\sum\limits_{n}(y_n - \bar{y})^2}}, \tag{6}$$

where x_n is the value of a given pixel and delay time, $\bar{x}$ is the mean of the entire array for that delay time, y_n is the value of another pixel and delay time, and $\bar{y}$ is the mean of the entire array at that delay time. The crystal model arrays and their corresponding model diffraction intensities were zero-padded on all sides of the 2D array to 512×512 pixels, before being cropped to 128×128 pixels for minimising $1 - r$.

The shape of the crystal was assumed to be constant throughout the delay time measurements, as the temperature rise in the Pd lattice is far from the melting temperature.

The synthesised nanoparticles have very low defect densities; thus, we assume there is no significant residual strain or lattice displacement present without laser perturbation. The phase, ψ, was added to the shape, s, creating a complex crystal function, $S = se^{i\psi}$ for each element in the array. The phase was modelled after a planar acoustic wave propagating through it, given by,

$$\psi(x, x_0, s_1, s_2) = \begin{cases} s_1(x - x_0), & x \leq x_0 \\ s_2(x - x_0), & x > x_0 \end{cases} \tag{7}$$

where x is the horizontal position in the array, x_0 is the peak position of the wave, relative to the centre of the crystal, with a fixed amplitude of π, s_1 is the positive slope leading to x_0 and s_2 is the negative slope descending from x_0. The parameter values are shown in Fig. 5, and additional horizontal and vertical shifts of the Bragg peak are shown in Fig. S11. This wave was applied to Fig. 4b and c, where peak splitting was observed.

The associated displacement along [111], $\mathbf{u_{111}}$, can be computed by [30],

$$\mathbf{u_{111}} = \frac{\psi}{|\mathbf{Q}|}, \tag{8}$$

where $\mathbf{Q}$ is the scattering vector. The experimental intensities were shifted such that their centre of mass was in the centre of the 128×128 array for the optimisation. The normalised intensity values less than 0.05 were excluded from the centre of mass calculation. Following the optimisation, this shift was added to the model using a phase ramp. Thus, the displacements we observe in Fig. 4 are relative to the crystal at negative delay times. The strain, $\varepsilon_{\mathbf{111}}$, can be computed by [30],

$$\varepsilon_{\mathbf{111}} = \nabla\psi \cdot \frac{\mathbf{Q}}{|\mathbf{Q}|^2}, \tag{9}$$

where the phase gradients were determined by taking the derivative of the complex exponential [46],

$$\frac{\partial\psi}{\partial j} = \mathrm{Re}\left(\frac{\partial e^{i\psi}}{\partial j} \Big/ ie^{i\psi}\right), \tag{10}$$

where $j \in \{x, y\}$ in the 2D model. The optimised shapes and phases were transformed to the laboratory coordinate frame [47].

VI. DATA AVAILABILITY

The raw data is publicly available at [48]. The data analysis was performed on the Maxwell cluster using JupyterHub [49]. The analysis scripts to reproduce the results are publicly available at [50].

ACKNOWLEDGMENTS

We acknowledge European XFEL in Schenefeld, Germany, for the provision of X-ray free-electron laser beamtime at Scientific Instrument MID (Materials Imaging and Dynamics) under proposal number 2798 and would like to thank Mohamed Youssef for his assistance. Samples were provided by Benjamin P. Williams in the lab of Chia-Kuang (Frank) Tsung at Boston College. Work at Brookhaven National Laboratory was supported by the U.S. Department of Energy, Office of Science, Office of Basic Energy Sciences, under Contract No. DESC0012704. Work performed at UCL was supported by EPSRC.

---

[1] R. Xu, H. Jiang, C. Song, J. A. Rodriguez, Z. Huang, C.-C. Chen, D. Nam, J. Park, M. Gallagher-Jones, S. Kim, S. Kim, A. Suzuki, Y. Takayama, T. Oroguchi, Y. Takahashi, J. Fan, Y. Zou, T. Hatsui, Y. Inubushi, T. Kameshima, K. Yonekura, K. Tono, T. Togashi, T. Sato, M. Yamamoto, M. Nakasako, M. Yabashi, T. Ishikawa, and J. Miao, Single-shot three-dimensional structure determination of nanocrystals with femtosecond x-ray free-electron laser pulses, Nature Communications **5**, 4061 (2014).

[2] S. Link and M. A. El-Sayed, Optical properties and ultrafast dynamics of metallic nanocrystals, Annual Review of Physical Chemistry **54**, 331 (2003).

[3] N. Joudeh, A. Saragliadis, G. Koster, P. Mikheenko, and D. Linke, Synthesis methods and applications of palladium nanoparticles: A review, Frontiers in Nanotechnology **Volume 4 - 2022**, 10.3389/fnano.2022.1062608 (2022).

[4] M. Kateb, M. Azadeh, P. Marashi, and S. Ingvarsson, Size and shape-dependent melting mechanism of pd nanoparticles, Journal of Nanoparticle Research **20**, 251 (2018).

[5] Z. Li and X. Meng, Recent development on palladium enhanced photocatalytic activity: A review, Journal of Alloys and Compounds **830**, 154669 (2020).

[6] J. Hohlfeld, S.-S. Wellershoff, J. Güdde, U. Conrad, V. Jähnke, and E. Matthias, Electron and lattice dynamics following optical excitation of metals, Chemical Physics **251**, 237 (2000).

[7] J. N. Clark, L. Beitra, G. Xiong, A. Higginbotham, D. M. Fritz, H. T. Lemke, D. Zhu, M. Chollet, G. J. Williams, M. Messerschmidt, B. Abbey, R. J. Harder, A. M. Korsunsky, J. S. Wark, and I. K. Robinson, Ultrafast three-dimensional imaging of lattice dynamics in individual gold nanocrystals, Science **341**, 56 (2013).

[8] T. A. Assefa, Y. Cao, S. Banerjee, S. Kim, D. Kim, H. Lee, S. Kim, J. H. Lee, S.-Y. Park, I. Eom, J. Park, D. Nam, S. Kim, S. H. Chun, H. Hyun, K. sook Kim, P. Juhas, E. S. Bozin, M. Lu, C. Song, H. Kim, S. J. L. Billinge, and I. K. Robinson, Ultrafast x-ray diffraction study of melt-front dynamics in polycrystalline thin films, Science Advances **6**, eaax2445 (2020).

[9] J. Antonowicz, A. Olczak, K. Sokolowski-Tinten, P. Zalden, I. Milov, P. Dzięgielewski, C. Bressler, H. N. Chapman, M. Chojnacki, P. Dłużewski, A. Rodriguez-Fernandez, K. Fronc, W. Gawełda, K. Georgarakis, A. L. Greer, I. Jacyna, R. W. E. van de Kruijs, R. Kamiński, D. Khakhulin, D. Klinger, K. M. Kosyl, K. Kubicek, K. P. Migdal, R. Minikayev, N. T. Panagiotopoulos, M. Sikora, P. Sun, H. Yousef, W. Zajkowska-Pietrzak, V. V. Zhakhovsky, and R. Sobierajski, Structural pathways for ultrafast melting of optically excited thin polycrystalline palladium films, Acta Materialia **276**, 120043 (2024).

[10] A. F. Suzana, R. Koch, L. Wu, T. A. Assefa, S. Kim, S. Choi, H. Lee, S. Kim, J. H. Lee, S. Y. Park, D. Nam, S. Kim, H. Hyun, K. S. Kim, G. Wright, E. S. Bozin, C. Song, H. Kim, S. J. Billinge, and I. K. Robinson, Compressive effects in melting of palladium thin films studied by ultrafast x-ray diffraction, Physical Review B **107**, 10.1103/PhysRevB.107.214303 (2023).

[11] J. N. Clark, L. Beitra, G. Xiong, D. M. Fritz, H. T. Lemke, D. Zhu, M. Chollet, G. J. Williams, M. M. Messerschmidt, B. Abbey, R. J. Harder, A. M. Korsunsky, J. S. Wark, D. A. Reis, and I. K. Robinson, Imaging transient melting of a nanocrystal using an x-ray laser, Proceedings of the National Academy of Sciences of the United States of America **112**, 7444 (2015).

[12] Y. Ihm, D. H. Cho, D. Sung, D. Nam, C. Jung, T. Sato, S. Kim, J. Park, S. Kim, M. Gallagher-Jones, Y. Kim, R. Xu, S. Owada, J. H. Shim, K. Tono, M. Yabashi, T. Ishikawa, J. Miao, D. Y. Noh, and C. Song, Direct observation of picosecond melting and disintegration of metallic nanoparticles, Nature Communications **10**, 2411 (2019).

[13] Y. Sun, C. Chen, T. J. Albert, H. Li, M. I. Arefev, Y. Chen, M. Dunne, J. M. Glownia, M. Jerman, M. Hoffmann, M. J. Hurley, M. Mo, Q. L. Nguyen, T. Sato, S. Song, P. Sun, M. Sutton,

S. Teitelbaum, A. S. Valavanis, N. Wang, D. Zhu, L. V. Zhigilei, and K. Sokolowski-Tinten, Dynamics of nanoscale phase decomposition in laser ablation, Communications Materials **6**, 69 (2025).

[14] J.-E. Pudell, M. Mattern, M. Hehn, G. Malinowski, M. Herzog, and M. Bargheer, Heat transport without heating?—an ultrafast x-ray perspective into a metal heterostructure, Advanced Functional Materials **30**, 2004555 (2020).

[15] J.-E. Pudell, A. A. Maznev, M. Herzog, M. Kronseder, C. H. Back, G. Malinowski, A. von Reppert, and M. Bargheer, Layer specific observation of slow thermal equilibration in ultrathin metallic nanostructures by femtosecond x-ray diffraction, Nature Communications **9**, 3335 (2018).

[16] N. Jourdain, L. Lecherbourg, V. Recoules, P. Renaudin, and F. Dorchies, Ultrafast thermal melting in nonequilibrium warm dense copper, Physical Review Letters **126**, 65001 (2021).

[17] M. Kandyla, T. Shih, and E. Mazur, Femtosecond dynamics of the laser-induced solid-to-liquid phase transition in aluminum, Physical Review B **75**, 214107 (2007).

[18] B. J. Siwick, J. R. Dwyer, R. E. Jordan, and R. J. D. Miller, An atomic-level view of melting using femtosecond electron diffraction, Science **302**, 1382 (2003), doi: 10.1126/science.1090052.

[19] M. Z. Mo, Z. Chen, R. K. Li, M. Dunning, B. B. L. Witte, J. K. Baldwin, L. B. Fletcher, J. B. Kim, A. Ng, R. Redmer, A. H. Reid, P. Shekhar, X. Z. Shen, M. Shen, K. Sokolowski-Tinten, Y. Y. Tsui, Y. Q. Wang, Q. Zheng, X. J. Wang, and S. H. Glenzer, Heterogeneous to homogeneous melting transition visualized with ultrafast electron diffraction, Science **360**, 1451 (2018), doi: 10.1126/science.aar2058.

[20] S. I. Anisimov, B. L. Kapeliovich, and T. L. Perelman, Electron emission from metal surfaces exposed to ultrashort laser pulses, Soviet Journal of Experimental and Theoretical Physics **39**, 375 (1974).

[21] J. K. Chen, D. Y. Tzou, and J. E. Beraun, A semiclassical two-temperature model for ultrafast laser heating, International Journal of Heat and Mass Transfer **49**, 307 (2006).

[22] Z. Lin and L. V. Zhigilei, Time-resolved diffraction profiles and atomic dynamics in short-pulse laser-induced structural transformations: Molecular dynamics study, Physical Review B **73**, 184113 (2006).

[23] K. Sokolowski-Tinten, C. Blome, C. Dietrich, A. Tarasevitch, M. H. von Hoegen, D. von der Linde, A. Cavalleri, J. Squier, and M. Kammler, Femtosecond x-ray measurement of ultrafast

melting and large acoustic transients, Physical Review Letters **87**, 225701 (2001).

[24] A. Olczak, R. Sobierajski, P. Dzięgielewski, S. A. Khan, Z. Kostera, K. P. Migdal, I. Milov, K. Sokolowski-Tinten, P. Zalden, V. V. Zhakhovsky, and J. Antonowicz, Atomic dynamics and local structural disorder during ultrafast melting of polycrystalline pd, Scripta Materialia **267**, 116826 (2025).

[25] L. Gelisio, Y. Y. Kim, S. W. Lim, D. Nam, I. Eom, M. Kim, S. Kim, R. Khubbutdinov, L. Xiang, H. Lee, M. Ree, C. U. Kim, and I. A. Vartanyants, Infrared-induced ultrafast melting of nanostructured platinum films probed by an x-ray free-electron laser, Physical Review B **110**, 144303 (2024).

[26] C. Thomsen, H. T. Grahn, H. J. Maris, and J. Tauc, Surface generation and detection of phonons by picosecond light pulses, Physical Review B **34**, 4129 (1986).

[27] D. Milathianaki, S. Boutet, G. J. Williams, A. Higginbotham, D. Ratner, A. E. Gleason, M. Messerschmidt, M. M. Seibert, D. C. Swift, P. Hering, J. Robinson, W. E. White, and J. S. Wark, Femtosecond visualization of lattice dynamics in shock-compressed matter, Science **342**, 220 (2013), doi: 10.1126/science.1239566.

[28] N. Medvedev and I. Milov, Electron-phonon coupling in metals at high electronic temperatures, Physical Review B **102**, 64302 (2020).

[29] M. Nicoul, U. Shymanovich, A. Tarasevitch, D. von der Linde, and K. Sokolowski-Tinten, Picosecond acoustic response of a laser-heated gold-film studied with time-resolved x-ray diffraction, Applied Physics Letters **98**, 191902 (2011).

[30] I. Robinson and R. Harder, Coherent x-ray diffraction imaging of strain at the nanoscale, Nature Materials **8**, 291 (2009).

[31] D. Sayre, Some implications of a theorem due to shannon, Acta Crystallographica **5**, 843 (1952).

[32] J. R. Fienup, Phase retrieval algorithms: a comparison, Applied Optics **21**, 2758 (1982).

[33] C. Kim, M. Scholz, and A. Madsen, The influence of strain on image reconstruction in bragg coherent x-ray diffraction imaging and ptychography, Journal of Synchrotron Radiation **28**, 1159 (2021).

[34] P. B. Johnson and R. W. Christy, Optical constants of transition metals: Ti, v, cr, mn, fe, co, ni, and pd, Physical Review B **9**, 5056 (1974).

[35] G. V. Samsonov, *Handbook of the physicochemical properties of the elements* (Plenum Publishing Corporation, New York, 1968).

[36] D. Schick, M. Herzog, A. Bojahr, W. Leitenberger, A. Hertwig, R. Shayduk, and M. Bargheer, Ultrafast lattice response of photoexcited thin films studied by x-ray diffraction, Structural Dynamics **1**, 064501 (2014).

[37] Y. Y. Chen, Y. D. Yao, S. S. Hsiao, S. U. Jen, B. T. Lin, H. M. Lin, and C. Y. Tung, Specific-heat study of nanocrystalline palladium, Physical Review B **52**, 9364 (1995).

[38] Z. Lin, L. V. Zhigilei, and V. Celli, Electron-phonon coupling and electron heat capacity of metals under conditions of strong electron-phonon nonequilibrium, Physical Review B **77**, 75133 (2008).

[39] A. F. Suzana, L. Wu, T. A. Assefa, B. P. Williams, R. Harder, W. Cha, C. H. Kuo, C. K. Tsung, and I. K. Robinson, Structure of a seeded palladium nanoparticle and its dynamics during the hydride phase transformation, Communications Chemistry **4**, 10.1038/s42004-021-00500-7 (2021).

[40] M. Monteforte, A. K. Estandarte, B. Chen, R. Harder, M. H. Huang, and I. K. Robinson, Novel silica stabilization method for the analysis of fine nanocrystals using coherent x-ray diffraction imaging, Journal of Synchrotron Radiation **23**, 953 (2016).

[41] A. Madsen, J. Hallmann, G. Ansaldi, T. Roth, W. Lu, C. Kim, U. Boesenberg, A. Zozulya, J. Moller, R. Shayduk, M. Scholz, A. Bartmann, A. Schmidt, I. Lobato, K. Sukharnikov, M. Reiser, K. Kazarian, and I. Petrov, Materials imaging and dynamics (mid) instrument at the european x-ray free-electron laser facility, Journal of Synchrotron Radiation **28**, 637 (2021).

[42] A. Allahgholi, J. Becker, A. Delfs, R. Dinapoli, P. Goettlicher, D. Greiffenberg, B. Henrich, H. Hirsemann, M. Kuhn, R. Klanner, A. Klyuev, H. Krueger, S. Lange, T. Laurus, A. Marras, D. Mezza, A. Mozzanica, M. Niemann, J. Poehlsen, J. Schwandt, I. Sheviakov, X. Shi, S. Smoljanin, L. Steffen, J. Sztuk-Dambietz, U. Trunk, Q. Xia, M. Zeribi, J. Zhang, M. Zimmer, B. Schmitt, and H. Graafsma, The adaptive gain integrating pixel detector at the european xfel, Journal of Synchrotron Radiation **26**, 74 (2019).

[43] J. Wrigley, DAMNIT, `https://damnit.readthedocs.io/en/latest/` (2025).

[44] T. Maltezopoulos, F. Dietrich, W. Freund, U. F. Jastrow, A. Koch, J. Laksman, J. Liu, M. Planas, A. A. Sorokin, K. Tiedtke, and J. Grünert, Operation of x-ray gas monitors at the european xfel, Journal of Synchrotron Radiation **26**, 1045 (2019).

[45] P. Virtanen, R. Gommers, T. E. Oliphant, M. Haberland, T. Reddy, D. Cournapeau, E. Burovski, P. Peterson, W. Weckesser, J. Bright, S. J. van der Walt, M. Brett, J. Wilson, K. J. Millman, N. Mayorov, A. R. J. Nelson, E. Jones, R. Kern, E. Larson, C. J. Carey, İlhan Polat, Y. Feng, E. W. Moore, J. VanderPlas, D. Laxalde, J. Perktold, R. Cimrman, I. Henriksen, E. A. Quintero, C. R. Harris, A. M. Archibald, A. H. Ribeiro, F. Pedregosa, P. van Mulbregt, A. Vijaykumar, A. P. Bardelli, A. Rothberg, A. Hilboll, A. Kloeckner, A. Scopatz, A. Lee, A. Rokem, C. N. Woods, C. Fulton, C. Masson, C. Häggström, C. Fitzgerald, D. A. Nicholson, D. R. Hagen, D. V. Pasechnik, E. Olivetti, E. Martin, E. Wieser, F. Silva, F. Lenders, F. Wilhelm, G. Young, G. A. Price, G.-L. Ingold, G. E. Allen, G. R. Lee, H. Audren, I. Probst, J. P. Dietrich, J. Silterra, J. T. Webber, J. Slavič, J. Nothman, J. Buchner, J. Kulick, J. L. Schönberger, J. V. de Miranda Cardoso, J. Reimer, J. Harrington, J. L. C. Rodríguez, J. Nunez-Iglesias, J. Kuczynski, K. Tritz, M. Thoma, M. Newville, M. Kümmerer, M. Bolingbroke, M. Tartre, M. Pak, N. J. Smith, N. Nowaczyk, N. Shebanov, O. Pavlyk, P. A. Brodtkorb, P. Lee, R. T. McGibbon, R. Feldbauer, S. Lewis, S. Tygier, S. Sievert, S. Vigna, S. Peterson, S. More, T. Pudlik, T. Oshima, T. J. Pingel, T. P. Robitaille, T. Spura, T. R. Jones, T. Cera, T. Leslie, T. Zito, T. Krauss, U. Upadhyay, Y. O. Halchenko, Y. Vázquez-Baeza, and S. . Contributors, Scipy 1.0: fundamental algorithms for scientific computing in python, Nature Methods **17**, 261 (2020).

[46] D. Yang, M. T. Lapington, G. He, K. Song, M. Zhang, C. Barker, R. J. Harder, W. Cha, W. Liu, N. W. Phillips, and F. Hofmann, Refinements for bragg coherent x-ray diffraction imaging: Electron backscatter diffraction alignment and strain field computation, Journal of Applied Crystallography **55**, 1184 (2022).

[47] D. Yang, N. W. Phillips, and F. Hofmann, Mapping data between sample and detector conjugated spaces in bragg coherent diffraction imaging, Journal of Synchrotron Radiation **26**, 2055 (2019).

[48] Laser-induced ultrafast melting of octahedral palladium nanocrystals, 10.22003/XFEL.EU-DATA-002798-00 (2022).

[49] H. Fangohr, M. Beg, M. Bergemann, V. Bondar, S. Brockhauser, A. Campbell, C. Carinan, R. Costa, F. Dall'Antonia, C. Danilevski, J. C. E, W. Ehsan, S. G. Esenov, R. Fabbri, S. Fangohr, E. F. del Castillo, G. Flucke, C. Fortmann-Grote, D. F. Marsa, G. Giovanetti, D. Goeries, A. Götz, J. Hall, S. Hauf, D. G. Hickin, T. H. Rod, T. Jarosiewicz, E. Kamil, M. Karnevskiy,

J. Kieffer, Y. Kirienko, A. Klimovskaia, T. A. Kluyver, M. Kuster, L. L. Guyader, A. Madsen, L. G. Maia, D. Mamchyk, L. Mercadier, T. Michelat, I. Mohacsi, J. Möller, A. Parenti, E. Pellegrini, J. F. Perrin, M. Reiser, J. Reppin, R. Rosca, D. B. Rück, T. Rüter, H. Santos, R. Schaffer, A. Scherz, F. Schlünzen, M. Scholz, M. Schuh, J. R. Selknaes, A. Silenzi, G. Sipos, M. Spirzewski, J. Sztuk, J. Szuba, J. W. Taylor, S. Trojanowski, K. Wrona, A. A. Yaroslavtsev, and J. Zhu, Data exploration and analysis with jupyter notebooks, in *International Conference on Accelerator and Large Experimental Physics Control Systems*, edited by K. S. White, K. A. Brown, P. S. Dyer, and V. R. W. Schaa (JACoW Publishing, 2020) pp. 799–806.

[50] 10.5281/zenodo.15319844 (2025).